JACS
JOURNAL OF THE AMERICAN CHEMICAL SOCIETY
Article
pubs.acs.org/JACS

# A Porphyrin-Based Molecular Tweezer: Guest-Induced Switching of Forward and Backward Photoinduced Energy Transfer

Hongsik Yoon, Jong Min Lim, Hyuk-Chan Gee, Chi-Hwa Lee, Young-Hwan Jeong, Dongho Kim,* and Woo-Dong Jang*

Department of Chemistry, Yonsei University, 50 Yonsei-ro, Seodaemoon-Gu, Seoul 120-749, Korea

Supporting Information

**ABSTRACT:** A bisindole-bridged-porphyrin tweezer (**1**), a pair of zinc porphyrins ($\mathbf{P_{Zn}}$'s) connected to bisindole bridge (**BB**) via the $Cu^{I}$-mediated alkyne−azide click chemistry, exhibited unique switching in forward and backward photoinduced energy transfer by specific guest bindings. The addition of $Cu^{2+}$ caused a change in electronic absorption and fluorescence quenching of **1**. MALDI-TOF-MS and FT-IR analyses indicated the formation of stable coordination complex between **1** and $Cu^{2+}$ (**1**-Cu(II)). Without $Cu^{2+}$ coordination, the excitation energy flows from **BB** to $\mathbf{P_{Zn}}$'s with significantly high energy transfer efficiency. In contrast, the direction of energy flow in **1** was completely reversed by the coordination of $Cu^{2+}$. The difference in fluorescence quantum yield between **1** and **1**-Cu(II) indicates that more than 95% of excitation energy of $\mathbf{P_{Zn}}$ flows into Cu(II)-coordinated **BB**. The energy transfer efficiency was further controlled by bidentate ligand coordination onto **1**-Cu(II). When pyrophosphate ion was added to **1**-Cu(II), the recovery of fluorescence emission from $\mathbf{P_{Zn}}$ was observed. The quantum mechanical calculations indicated that the Cu(II)-coordinated **BB** has square planar geometry, which can be distorted to form octahedral geometry due to the coordination of bidentate ligands.

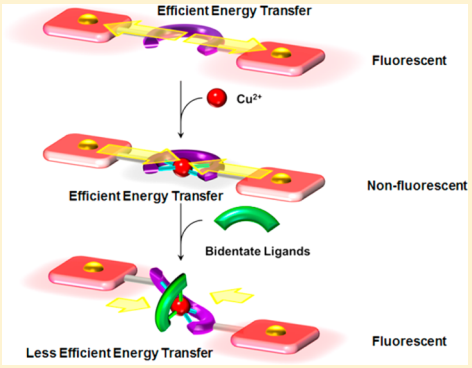


## INTRODUCTION

The photoinduced energy transfer is a decisive process in the light-energy conversion of natural light harvesting system.[1−3] The photochemical reaction in the light harvesting complex is usually initiated by the light absorption by pigment array and successive vectorial energy transfer to the reaction center.[4] The vectorial energy transfer phenomena gave great inspiration for the design in artificial photofunctional devices, including photovoltaic, electroluminescent, and biomedical devices.[5−15] The natural light harvesting involves obviously much more complicated mechanisms than artificial ones for the precise regulation of light−energy conversion. For example, plants and bacteria have evolved photoprotective mechanisms to avoid an overexpose to strong light because the reactive oxygen species generated during photosynthesis are harmful to damage the photosynthetic system itself.[3,16−18] The natural photosynthetic systems are composed of various molecular accessories which are utilized for the regulation of light harvesting process by the supramolecular complex formation with specific proteins or ionic species.[19−23] Typically, the metal ion bindings to the light harvesting antenna give significant influences on the efficiency and dynamics of photosynthesis.[24−27] Although the continuous efforts by synthetic chemists enable the establishment of the directional energy transfer through the conjugation of donor−acceptor pairs,[28−32] the examples of guest specific control of photoinduced energy transfer are still very rare.[33] In this study, we have newly designed a bisindole-bridged-porphyrin tweezer (**1**; Chart 1) with $Cu^{I}$-mediated alkyne−azide click chemistry, which exhibited unique photoluminescence switching phenomena by specific guest bindings.

## EXPERIMENTAL SECTION

**Materials and Measurements.** All commercially available reagents were reagent grade and used without further purification. Dichloromethane, *n*-hexane, and tetrahydrofuran (THF) were freshly distilled before each use. UV/vis absorption and fluorescence emission spectra were recorded with a JASCO V-660 spectrophotometer and

**Chart 1. Structures of Bisindole-Bridged-Porphyrin Tweezer (1) and Bisindole-Bridge (2)**

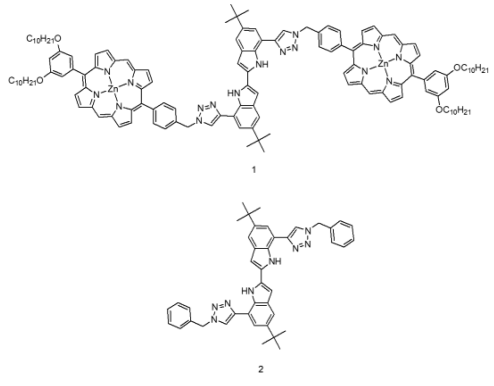

**Received:** December 11, 2013
**Published:** January 8, 2014




dx.doi.org/10.1021/ja4124048 | J. Am. Chem. Soc. 2014, 136, 1672−1679

JASCO FP-6300 spectrofluorometer, respectively. A time-correlated single-photon-counting (TCSPC) system was used for measurement of spontaneous fluorescence decay. The excitation and probe wavelengths were 400 and 650 nm for **1**, and 370 and 400 nm for **2**, respectively. As an excitation light source, we used a mode-locked Ti:sapphire laser (Spectra Physics, MaiTai BB) which provides ultrashort pulse (80 fs at full width half-maximum, fwhm) of 800 nm. The output pulse was frequency-doubled by a 1 mm thickness of a BBO crystal (EKSMA). The fluorescence was collected by a microchannel plate photomultiplier with a thermoelectric cooler connected to a TCSPC board (Becker & Hickel SPC-130).[34] Femtosecond (fs) time-resolved transient absorption (TA) spectra were recorded using a spectrometer consisting of a homemade noncollinear optical parametric amplifier (NOPA) pumped by a Ti:sapphire regenerative amplifier system (Quantronix, Integra-C) operating at 1 kHz repetition rate coupled with an optical detection system. The generated visible NOPA pulses had a pulse width of ∼100 fs and an average power of 1 mW in the range 480−700 nm, which were used as pump pulses. White light continuum (WLC) probe pulses were generated using a sapphire window (2 mm of thickness) by focusing of small portion of the fundamental 800 nm pulses that were picked off by a quartz plate before entering into the NOPA. The time delay between pump and probe beams was carefully controlled by causing the pump beam to travel along a variable optical delay (Newport, ILS250).[35] $^1$H and $^{13}$C NMR spectra were recorded on a Bruker Avance DPX 250 and DPX 400 spectrometer, respectively, at 25 °C in [$D_8$]THF, or $CDCl_3$. MALDI-TOF-MS was performed on Bruker Daltonics LRF20 with dithranol (1,8,9-trihydroxyanthracene) as the matrix. FT-IR was performed on Bruker Vertax 70 (the specimens were prepared by drop-casting of a THF solution onto $CaF_2$ window).

**Estimation of Quantum Yield.** The quantum yield can be calculated from followed equation:

$$\Phi_f^i = \frac{F^i f_s n_i^2}{F^s f_i n_s^2}\Phi_f^s$$

where $\Phi_f^i$ and $\Phi_f^s$ are the photoluminescence quantum yields of the sample and standard, respectively. The subscript f is used because in most cases one is dealing with fluorescence. The $F^i$ and $F^s$ are the integrated intensities (areas) of sample and standard spectra, respectively (in units of photons). The $f_x$ is the absorption factor (also known under the obsolete term "absorptance"), the fraction of the light impinging on the sample that is absorbed ($f_x = 1 - 10^{-A_x}$, where $A$ = absorbance). The $n_i$ and $n_s$ are the reflective indexes of the solvents for sample and standard, respectively. As reference compounds, 5,10,15,20-tetraphenylporphyrin ($\lambda_{ex}$ = 420 nm, $\Phi$ = 0.12 in toluene) and anthracene ($\lambda_{ex}$ = 342 nm, $\Phi$ = 0.27 in ethanol) were utilized for the determination of quantum yields of **1** and **2**, respectively.[36]

**Molecular Modeling Study.** Quantum mechanical calculations were performed using the Gaussian09 program suite. All calculations were carried out using density functional theory (DFT) with the unrestricted Becke's three-parameter hybrid exchange functional and the Lee−Yang−Parr correlation functional (UB3LYP), employing a basis set of lanl2dz for all atoms. Molecular dynamic calculations were carried out by CAChe7.5 using MM2 force field.

**Synthesis.** The synthetic procedure of **1** and **2** are outlined in Scheme 1. Hydroxy-group-bearing porphyrin (**$P_{Zn}$−OH**), bromide-bearing porphyrin (**$P_{Zn}$−Br**) and ethynyl-bearing bisindole (**Ethynyl−BB**) were synthesized according to the literature procedure.[8,9,37] Azide-bearing porphyrin (**$P_{Zn}$-$N_3$**) was prepared by azidation of **$P_{Zn}$−Br**. The $Cu^I$-mediated click reaction between **$P_{Zn}$−$N_3$** and **Ethynyl−BB** resulted in **1**, which was unambiguously characterized by $^1$H, $^{13}$C NMR, and MALDI-TOF-MS analyses. Similarly, the click reaction between **Ethynyl−BB** and benzyl azide resulted in bisindole-bridge (**BB**) without porphyrin units (**2**) as a structural fragment.

**$P_{Zn}$−$N_3$**: $NaN_3$ (0.50 g, 7.70 mmol) was added to a solution of **$P_{Zn}$−Br** (1.20 g, 1.28 mmol) in a 15 mL THF/$H_2O$ mixture (4:1). The resulting suspension was stirred for 9 h at 25 °C, and the reaction

**Scheme 1. Synthesis of Porphyrin-Based Molecular Tweezer**

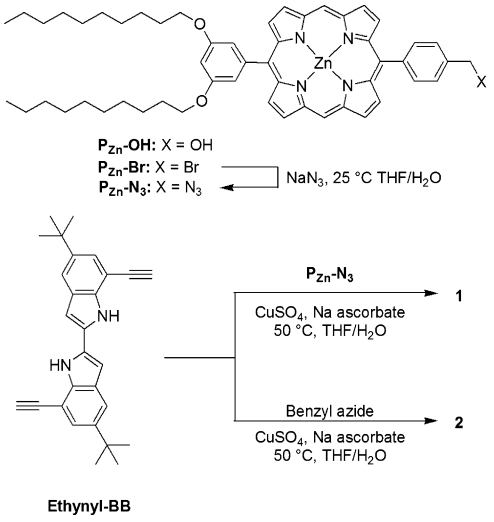


mixture was evaporated to dryness. The residue was purified using column chromatography with 50% $CH_2Cl_2$/hexane as an eluent to produce **$P_{Zn}$−$N_3$** as a purple solid (1.00 g, 87%). $^1$H NMR (400 MHz, $CDCl_3$, 25 °C) $\delta$ = 10.07 (s, 2 H), 9.35−9.34 (d, $J$ = 4.4 Hz, 2 H), 9.29−9.28 (d, $J$ = 4.8 Hz, 2 H), 9.22−9.21 (d, $J$ = 4.4 Hz, 2 H), 8.86−8.85 (d, $J$ = 4.4 Hz, 2 H), 7.99−7.97 (d, $J$ = 7.6 Hz, 2H), 7.48 (s, 2 H), 7.02−7.00 (d, $J$ = 8 Hz, 2 H), 6.91 (s, 1 H), 4.15−4.12 (t, $J$ = 6.4 Hz, 4 H), 3.50 (s, 2 H), 1.90−1.29 (m, 32 H), 0.94−0.90 ppm (t, 6.4 Hz, 6 H). MALDI-TOF-MS $m/z$: calcd for $C_{53}H_{61}N_7O_2Zn$, 893.51 [$M^+$]; found, 891.85.

**1**: $CuSO_4 \cdot 5H_2O$ (7 mg, 0.03 mmol) and sodium ascorbate (11 mg, 0.06 mmol) were added to a mixture of **Ethynyl−BB** (20 mg, 0.05 mmol) and **$P_{Zn}$−$N_3$** (259 mg, 0.29 mmol) in 7 mL THF/$H_2O$ (1:1). The reaction mixture was stirred for 7 h at 50 °C, and then the organic layer was separated, dried over $MgSO_4$, and filtered. After evaporation of the solvent under reduced pressure, the residue was purified using column chromatography with 70% $CH_2Cl_2$/hexane, as an eluent and evaporated to dryness. The residue was recrystallized from $CH_2Cl_2$/hexane to produce **1** as a purple solid (90 mg, 83%). $^1$H NMR(400 MHz, [$D_8$]THF, 25 °C) $\delta$ = 11.15 (s, 2 H), 10.23 (s, 4 H), 9.38−9.36 (t, $J$ = 4.8 Hz, 8 H), 9.15−9.14 (d, $J$ = 4.4 Hz, 4 H), 9.03−9.02 (d, $J$ = 4.4 Hz, 4 H), 8.80 (s, 2 H), 8.31−8.29 (d, $J$ = 7.6 Hz, 4 H), 7.87−7.85 (d, $J$ = 7.6 Hz, 4 H), 7.74 (s, 2 H), 7.70 (s, 2 H), 7.40 (s, 4 H), 7.07 (s, 2 H), 6.94 (s, 2 H), 6.13 (s, 4 H), 4.18−4.15 (t, $J$ = 6.4 Hz, 8 H), 1.89−1.28 (m, 32 H), 0.88−0.85 ppm (t, $J$ = 6.4 Hz, 12 H). $^{13}$C NMR (100 MHz, [$D_8$]THF, 25 °C) $\delta$ = 159.60, 151.00, 150.81, 150.78, 150.62, 149.48, 146.04, 144.69, 143.55, 136.44, 136.25, 133.90, 133.25, 133.03, 132.64, 132.44, 132.31, 131.43, 127.04, 121.36, 120.68, 119.61, 118.10, 117.29, 115.63, 114.57, 106.61, 101.26, 100.32, 69.03, 54.79, 35.52, 33.03, 32.63, 30.78, 30.72, 30.62, 30.46, 27.32, 23.72, 14.60 ppm. MALDI-TOF-MS $m/z$: calcd for $C_{134}H_{150}N_{16}O_4Zn_2$, 2179.55 [$M^+$]; found, 2180.42; $\varepsilon_{412.5\ nm}$ = 559 000.

**2**: $CuSO_4 \cdot 5H_2O$ (7 mg, 0.03 mmol) and sodium ascorbate (11 mg, 0.06 mmol) were added to a mixture of **Ethynyl−BB** (20 mg, 0.05 mmol) and benzyl azide (38.61 mg, 0.29 mmol) in 7 mL THF/$H_2O$ (1:1). The reaction mixture was stirred for 7 h at 50 °C, and then the organic layer was separated, dried over $MgSO_4$, and filtered. After evaporation of the solvent under reduced pressure, the residue was purified using column chromatography with $CH_2Cl_2$, and evaporated to dryness. The residue was recrystallized from $CH_2Cl_2$/hexane to produce **2** as a white solid (30 mg, 91%). $^1$H NMR(400 MHz, $CDCl_3$, 25 °C) $\delta$ = 10.69 (s, 2 H), 7.92 (s, 2 H), 7.64 (s, 2 H), 7.52−7.36 (m, 12 H), 6.93 (s, 2 H), 5.67 (s, 4 H), 1.41 ppm (s, 18 H). $^{13}$C NMR (100 MHz, $CDCl_3$, 25 °C) $\delta$ = 148.26, 141.95, 135.94, 135.09, 129.38, 128.95, 128.33, 124.03, 120.47, 119.36, 116.62, 112.86, 54.56, 34.93, 32.30 ppm. MALDI-TOF-MS $m/z$: calcd for $C_{42}H_{42}N_8$, 658.84 [$M^+$]; found, 659.39.


dx.doi.org/10.1021/ja4124048 | J. Am. Chem. Soc. 2014, 136, 1672−1679

**Metal Coordination and Ligand Binding Experiments.** Solutions of various metal salts in THF (2.0 mM, 10 $\mu$L) were added to THF solution of **1** and **2** (2.0 $\mu$M, 2.0 mL), and visual changes and fluorescence emission changes were observed to test the capability of metal coordination. The fluorescence emission change was observed upon 350 nm irradiation by UV handy lamp (ex: 360 nm, VILBER LOURMAT, VL-4LC). For the UV/vis and fluorescence titration studies, 10 and 1 × $10^2$ $\mu$M solution of $Cu(ClO_4)_2$ in THF was successively added to THF solution of **1** (2.0 $\mu$M) and **2** (20 $\mu$M), respectively, and spectral changes were monitored using spectrophotometer. THF solutions of several anionic species, 2,2-bipyridine, and 1,3-bis(diphenylphosphino)propane were added to a mixture solution of **1** (2.0 $\mu$M) and $Cu(ClO_4)_2$ (4.0 $\mu$M), and the fluorescence and absorption changes were monitored for the evaluation of additional ligand bindings. The same experiment was carried out to the mixture solution of **2** (20 $\mu$M) and $Cu(ClO_4)_2$ (40 $\mu$M).

## RESULTS AND DISCUSSION

Figure 1 shows the electronic absorption and fluorescence emission spectra of **1** and **2** (2.0 and 20 $\mu$M in THF, respectively). Compound **1** exhibits strong absorption around 412 nm, corresponding to the B band of zinc porphyrin ($\mathbf{P_{Zn}}$). Compound **2** exhibits absorption around 350 nm with some vibronic bands. Upon excitation at 342 nm, **2** emits strong fluorescence around 400 nm ($\tau$ = 1.2 ns, $\Phi$ = 89.9%). The emission band of **2** partially overlaps with the B band absorption of $\mathbf{P_{Zn}}$ (see shaded area in Figure 1). Therefore, effective Förster type energy transfer from **BB** to $\mathbf{P_{Zn}}$'s can be expected. In fact, the fluorescence emission from **BB** was almost negligible in **1**, but strong emissions around 580 and 640 nm appeared upon 350 nm excitation. Moreover, the excitation spectra of **1** monitored at 637 nm, fluorescence from $\mathbf{P_{Zn}}$, showed the overlap of $\mathbf{P_{Zn}}$ and **BB** absorption (Figure S1). As control experiments, the absorption and fluorescence emission of **1** was compared with a noncovalent reference system, a 1:2 mixture of **2** and $\mathbf{P_{Zn}}$**–OH** in THF. Although both **1** and the noncovalent reference exhibited similar absorption (Figure S2), the noncovalent reference predominantly emitted strong fluorescence around 400 nm (Figure 2), indicating the energy transfer does not take place in the noncovalent reference system. When the relative intensity of fluorescence emission around 400 nm was compared, **1** exhibited less than 1% of fluorescence intensity in comparison with the noncovalent reference, indicating the excitation energy transfer efficiency from **BB** to $\mathbf{P_{Zn}}$ units is significantly high.

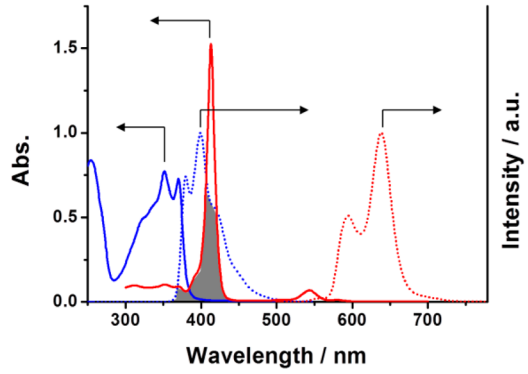


**Figure 1.** Absorption (solid line) and fluorescence (dotted line) spectra of **1** (red, 2.0 $\mu$M) and **2** (blue, 20 $\mu$M), where $\lambda_{ex}$ = 342 and 350 nm for **1** and **2**, respectively.

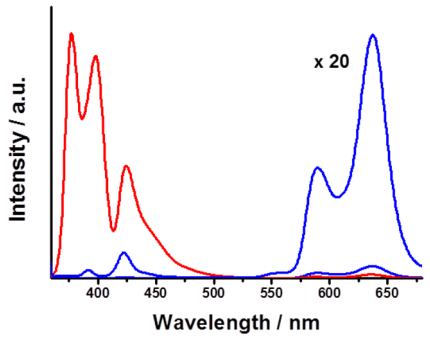


**Figure 2.** Fluorescence spectra of **1** (blue; 2.0 $\mu$M, $\lambda_{ex}$ = 350 nm) and noncovalent reference (red; 1:2 mixture of **2** and $\mathbf{P_{Zn}}$**–OH**, $\lambda_{ex}$ = 350 nm).

Because the indolic and triazole nitrogen atoms are potential metal coordination sites, we have tested the capability of metal binding into **BB**. To THF solutions of **1** and **2** (2.0 $\mu$M) were added 5 equiv of several metal cations and visual changes of color and emission were monitored. The addition of $Cu(ClO_4)_2$ caused a slight color change of the solution (Figure 3a). The same changes were observed when $Cu(OAc)_2$ was added instead of $Cu(ClO_4)_2$, indicating that the color change of the solution was caused by the interaction between **1** and $Cu^{2+}$ ion. Therefore, the electronic absorption and fluorescence spectra of **1** in THF were recorded upon successive addition of $Cu(ClO_4)_2$. Upon the addition of $Cu(ClO_4)_2$, **1** exhibited gradual decrease in the absorption around 350 nm and concomitant increase in the absorption around 495 nm (Figure 4a). The same spectral changes with isosbestic points at 302 and 380 nm have also been observed for **2** (20.0 $\mu$M) by addition of $Cu(ClO_4)_2$, indicating the binding site of $Cu^{2+}$ is not related with $\mathbf{P_{Zn}}$'s (Figure 4b). The continuous variation method (Job's plot)[38] indicated 1:1 complex formation for both **1** and **2** with $Cu^{2+}$ ion. The formation of Cu(II) coordinated complexes has been directly confirmed by MALDI-TOF-MS analysis. MALDI-TOF-MS spectrum of **1** exhibited a peak at $m/z$ = 2180.42, corresponding to $[\mathbf{1} + H]^+$. The Cu(II)-coordinated complexes of **1** (**1**-Cu(II)) formed by the additions of $Cu(OAc)_2$ and $Cu(ClO_4)_2$ exhibited nearly the same $m/z$ values at 2241.56 and 2241.44, respectively. Notably, the observed $m/z$ value for **1**-Cu(II) was less than 0.02% deviated from the calculated value for $[C_{134}H_{148}CuN_{16}O_4Zn_2]^+$, which is corresponding to the molecular formula for $[\mathbf{1} - 2H + Cu]^+$, indicating the deprotonation of indolic protons at **BB** to provide the coordination sites for $Cu^{2+}$ (Figure 5). The

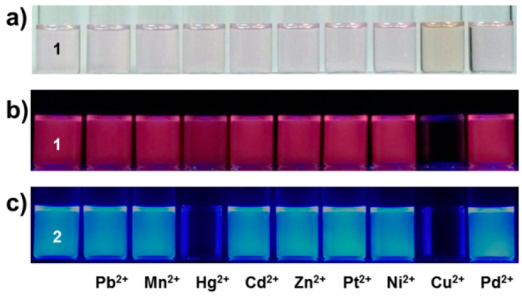


**Figure 3.** Color change of (a) **1**, and fluorescence change of (b) **1** and (c) **2** by addition of various metal ions as form of following salts, $Pb(ClO_4)_2{\cdot}2H_2O$, $Mn(OAc)_2$, $Hg(OAc)_2$, $Cd(NO_3)_2{\cdot}4H_2O$, $Zn(OAc)_2$, $PtCl_2$, $Ni(OAc)_2{\cdot}4H_2O$, $Cu(ClO_4)_2{\cdot}6H_2O$, $Pd(OAc)_2$.


dx.doi.org/10.1021/ja4124048 | J. Am. Chem. Soc. 2014, 136, 1672–1679

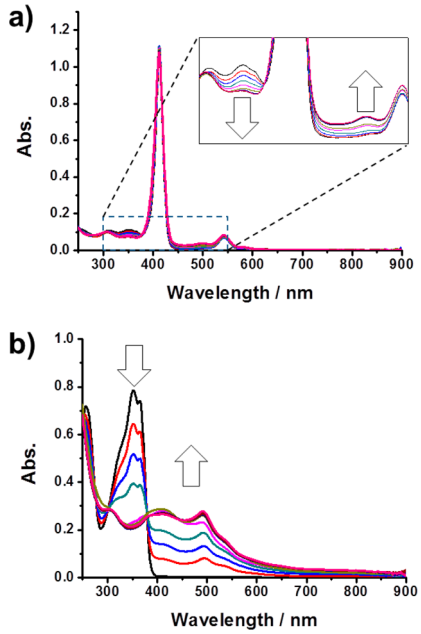


**Figure 4.** Absorption changes of (a) **1** (2.0 $\mu$M) and (b) **2** (20 $\mu$M) by successive addition of $Cu(ClO_4)_2$ (0–2.0, 0.25 equiv intervals).

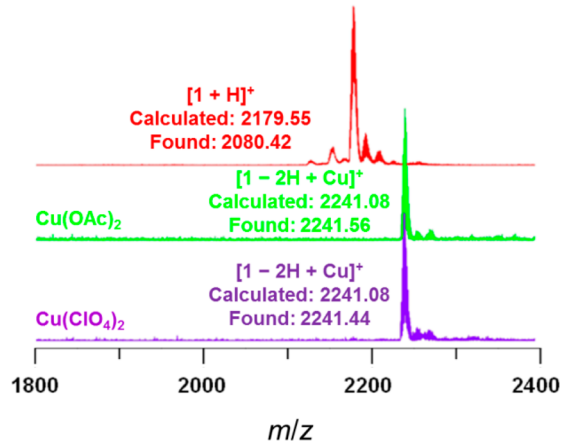


**Figure 5.** MALDI-TOF-MS spectra of **1** and **1**-Cu(II) complexes obtained by addition of $Cu(OAc)_2$ and $Cu(ClO_4)_2$.

MALDI-TOF-MS analysis for Cu(II)-coordinated complexes of **2** (**2**-Cu(II)) also showed the same aspect (Figure S3). FT-IR measurement of **1** and **2** also exhibited the disappearance of NH stretching band at 3400 $cm^{-1}$ by the formation of Cu(II)-coordinated complexes (Figure S4), reassuring the deprotonation of indolic protons. Due to the paramagnetic nature of $Cu^{2+}$ ion, the $^1H$ NMR spectrum of **1** was also greatly broadened by the formation of **1**-Cu(II) (Figure S5).

As mentioned above, the fluorescence emission of $\mathbf{P_{Zn}}$ completely disappeared by the formation of **1**-Cu(II) complex (Figures 3b and 6a), where the fluorescence quantum yields of **1** and **1**-Cu(II) were estimated to be 7.3 and 0.4%, respectively. Similarly, the fluorescence emission of **2** around 398 nm ($\tau$ = 1.2 ns, $\Phi$ = 89.9%) completely disappeared by the addition of $Cu^{2+}$ (Figures 3c and 6b), where the fluorescence quantum yield for **2**-Cu(II) was estimated to be less than 0.1%. Such fluorescence quenching phenomena of **2** was also observed by the addition of $Hg^{2+}$, indicating that $Hg^{2+}$ can be coordinated into the **BB** (Figures 3c and 7). However, all other metal ion

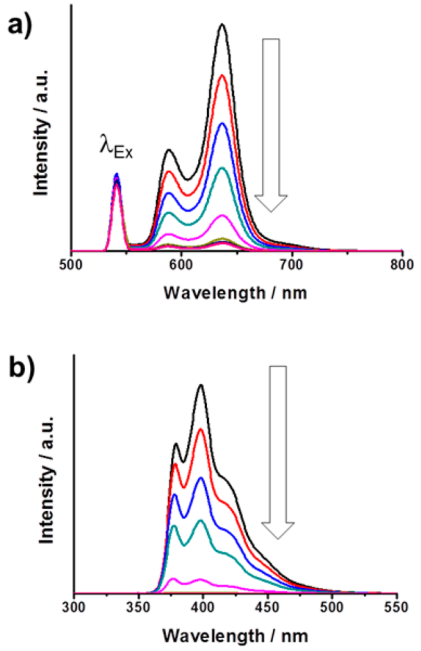


**Figure 6.** Fluorescence emission changes of (a) **1** (20 $\mu$M; $\lambda_{ex}$ = 542 nm) and (b) **2** (20 $\mu$M; $\lambda_{ex}$ = 350 nm) by successive addition of $Cu(ClO_4)_2$ (0–2.0, 0.25 equiv intervals).

additions, $Pb^{2+}$, $Mn^{2+}$, $Cd^{2+}$, $Zn^{2+}$, $Pt^{2+}$, $Ni^{2+}$, and $Pd^{2+}$, did not influence on the absorption as well as the emission of both **1** and **2**, indicating those metal ions cannot bind to the **BB** (Figure 7). Although the coordination of $Hg^{2+}$ to **2** caused a complete fluorescence quenching, the addition of $Hg^{2+}$ to **1** did not affect the fluorescence emission upon Q-band excitation of $\mathbf{P_{Zn}}$ (Figures 3c and 7). When we consider the molecular structure of **1**, the fluorescence emission of $\mathbf{P_{Zn}}$ cannot be directly affected by metal coordination because there is no $\pi$-conjugation between **BB**, the metal coordination site, and $\mathbf{P_{Zn}}$'s. Therefore, we need to consider a new mechanism to explain the fluorescence quenching of $\mathbf{P_{Zn}}$'s in **1**-Cu(II).

The structural optimization of metal-coordinated **BB** was carried out by the DFT calculations using the uB3LYP/Lanl2dz parameters. Figure 8 shows the optimized structure of **2**-Cu(II) and **2**-Hg(II) complexes with frontier molecular orbitals. The nonfluorescent characteristics of **2**-Cu(II) and **2**-Hg(II) complexes can be explained by the ligand to metal charge transfer (LMCT)[39,40] and the heavy atom effect,[41] respectively. The broad absorption band around 500 nm of **2**-Cu(II) complex is assignable to the LMCT band of square planar Cu(II) complex. The structural optimization of **2**-Cu(II) complex also exhibited the square planar geometry, where the central metal ion is surrounded by 4 nitrogen atoms belonging to 5-memberd aromatic rings. The HOMO of **2**-Cu(II) complex is predominantly delocalized on the **BB** moiety, whereas the LUMO of beta spin state is delocalized around the metal center, reinforcing the fluorescence quenching by LMCT. From the geometrical viewpoint, this square planar **2**-Cu(II) complex might be the pseudoporphyrin structure that has partially expanded aromatic characters. The bond lengths between metal ion and nitrogen atoms estimated by the DFT calculations are also very close to that of typical porphyrin structure (Figure 9). Although the structural optimization of **2**-Hg(II) complex showed the square planar geometry, it exhibited relatively longer metal to ligand bond lengths than


dx.doi.org/10.1021/ja4124048 | J. Am. Chem. Soc. 2014, 136, 1672–1679

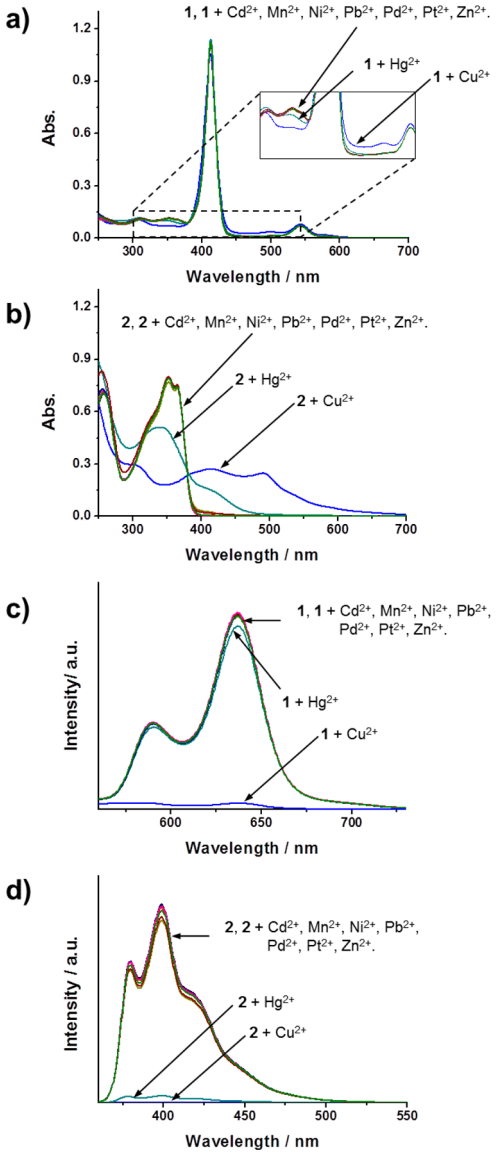


**Figure 7.** Spectral changes of **1** and **2** by 2 equiv of various metal ion addition. Absorption changes of (a) **1** (2.0 $\mu$M) and (b) **2** (20 $\mu$M), and fluorescence changes of (c) **1** (2.0 $\mu$M) and (d) **2** (20 $\mu$M). All spectra were measured after 10 min of metal additions.

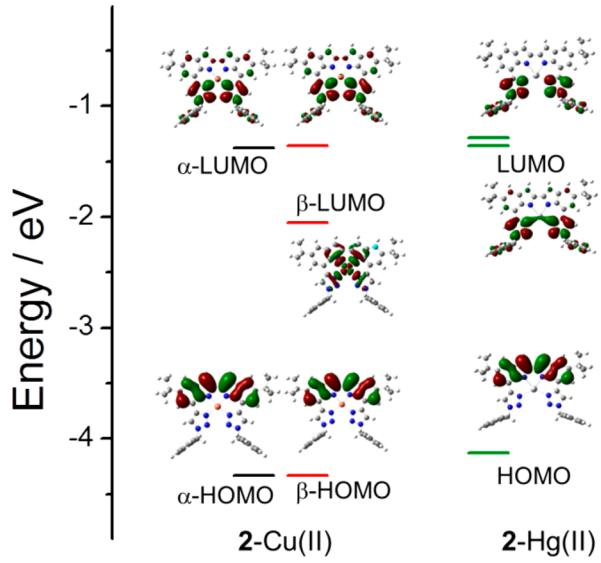


**Figure 8.** Energy diagram and frontier molecular orbitals of **2**-Cu(II) and **2**-Hg(II) estimated by DFT calculation.

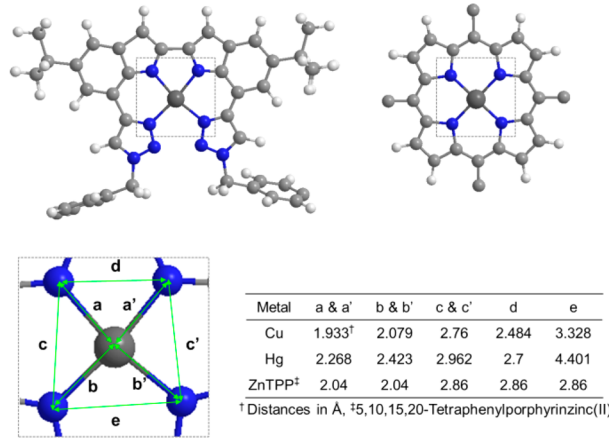


| Metal | a & a' | b & b' | c & c' | d | e |
|---|---|---|---|---|---|
| Cu | 1.933† | 2.079 | 2.76 | 2.484 | 3.328 |
| Hg | 2.268 | 2.423 | 2.962 | 2.7 | 4.401 |
| ZnTPP‡ | 2.04 | 2.04 | 2.86 | 2.86 | 2.86 |

† Distances in Å, ‡5,10,15,20-Tetraphenylporphyrinzinc(II)

**Figure 9.** Comparison of metal-coordinated **BB** and typical metalloporphyrin. Distances among metal and coordinated nitrogen atoms are summaries in table.

those in **2**-Cu(II) complex. The energy level and electronic distribution of HOMO of **2**-Hg(II) complex were very close to those of **2**-Cu(II) complex, whereas the electronic distribution of LUMO is predominantly delocalized over triazole rings in **2**-Hg(II).

The fluorescence quenching of $\mathbf{P}_{Zn}$'s in **1**-Cu(II) can be explained by energy transfer from $\mathbf{P}_{Zn}$'s to the $Cu^{2+}$-coordinated **BB**. The DFT geometry optimization indicated that the $Cu^{2+}$-coordinated **BB** adopted pseudoporphyrin structure, which may have partially expanded aromatic characters. In fact, the absorption spectrum of **2**-Cu(II) was widely spread over long wavelength region. In contrast, the absorption spectrum of **2**-Hg(II) exhibited only a small shoulder around 420 nm. The HOMO−LUMO band gaps estimated by the DFT calculations are also consistent with the electronic absorptions of both **2**-Cu(II) and **2**-Hg(II), where the HOMO−LUMO band gaps for **2**-Cu(II) and **2**-Hg(II) were estimated to be 2.29 (543 nm) and 2.98 eV (420 nm), respectively. Therefore, the effective overlap between the emission band of $\mathbf{P}_{Zn}$ and the absorption of Cu(II)-coordinated **BB** may facilitate the effective excitation energy transfer. In contrast, the excitation energy of $\mathbf{P}_{Zn}$'s in **1**-Hg(II) is difficult to be transferred to the core $Hg^{2+}$-coordinated **BB** due to its higher energy level. Because the LUMO of $\beta$ spin state in the $Cu^{2+}$-coordinated **BB** is delocalized around the metal center, the transferred energy from $\mathbf{P}_{Zn}$'s would directly flow to the central $Cu^{2+}$ ion and dissipate via nonradiative pathways.

Femtosecond time-resolved fluorescence and transient absorption measurements were conducted for **1** and **2**. The excitation and probe wavelengths for the time-resolved florescence measurements are 400 and 650 nm for **1**, and 370 and 400 nm for **2**, respectively (Figure S6). The fluorescence lifetime of **1** was determined to be 2.5 ns as single exponential decay, which is corresponding to that of typical $\mathbf{P}_{Zn}$ derivatives. The fluorescence lifetime of **2** was estimated to be 1.2 ns. Figure 10 shows transient absorption spectra and decay profiles of **1**, **2**, **1**-Cu(II), and **2**-Cu(II). The excitation wavelength of **1** and **1**-Cu(II) was 540 nm, which is in resonance with the Q-band absorption of $\mathbf{P}_{Zn}$. The transient


dx.doi.org/10.1021/ja4124048 | J. Am. Chem. Soc. 2014, 136, 1672−1679

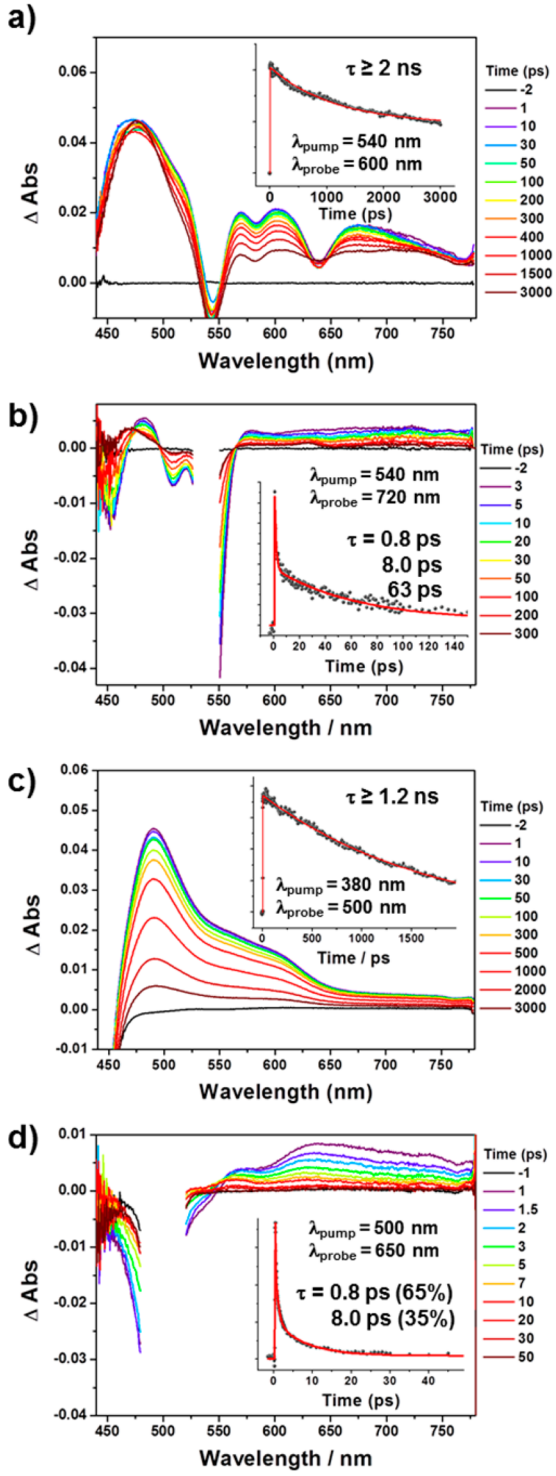


**Figure 10.** Femtosecond-transient absorption spectra and decay profiles of (a) **1**, (b) **1**-Cu(II), (c) **2**, and (d) **2**-Cu(II) in THF.

absorption spectra of **2** and **2**-Cu(II) were obtained upon excitation at 380 and 500 nm, respectively. The singlet excited state ($S_1$) lifetimes of both **1** and **2**, estimated from femtosecond-transient absorption measurements, are consistent with the fluorescence lifetimes. By the coordination of $Cu^{2+}$, the $S_1$ lifetime of **2** was greatly shortened where the values were estimated to be 0.8 (65%) and 8.0 ps (35%). Such fast decay dynamics was again observed in **1**-Cu(II) complex, but the major component of $S_1$ lifetime was estimated to be 63 ps, which is greatly reduced value compare with that of **1**. Because the transient absorption spectra of **1**-Cu(II) complex did not show any characteristic absorption bands of cationic radical species of $\mathbf{P}_{Zn}$, the reduced $S_1$ lifetime reinforces the excitation energy transfer from $\mathbf{P}_{Zn}$'s to the nonfluorescent Cu(II)-coordinated **BB** complex. As mentioned above, the square planar Cu(II)-coordinated **BB** resembles the porphyrin structure that has partially expanded aromatic characteristics, which can be an excellent energy acceptor. The reduced $S_1$ lifetime, as well as fluorescence quantum yield changes of **1** by the formation **1**-Cu(II) complex, indicate, that more than 95% of excitation energy of $\mathbf{P}_{Zn}$ flows into Cu(II)-coordinated **BB**. Because **1** originally exhibited directional energy flow from **BB** to $\mathbf{P}_{Zn}$'s with significantly high energy transfer efficiency, we can conclude here that the coordination of $Cu^{2+}$ to **BB** almost exclusively changes the energy transfer direction from forward to backward direction.

Another interesting aspect was observed when pyrophosphate (PPi) was added to **1**-Cu(II) complex (Figures 11 and

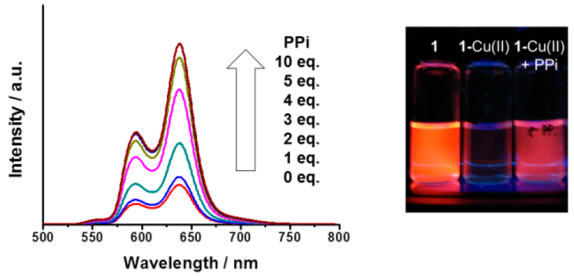


**Figure 11.** Florescence change of **1**-Cu(II) by addition of PPi.

S7). The spectral changes of **1**-Cu(II) complex were recorded upon addition of several anionic species as potential ancillary ligands. As a result, the fluorescence emission from $\mathbf{P}_{Zn}$ in **1**-Cu(II) was gradually recovered by the successive addition of PPi (Figure 11). The fluorescence lifetime of **1**-Cu(II) was also recovered to 2.1 ns (Figure S6). In contrast, no fluorescence emission from **2**-Cu(II) has been observed even after excess addition of PPi, indicating that the fluorescence enhancement of $\mathbf{P}_{Zn}$'s in **1**-Cu(II) is not caused by demetalation (Figure S8). Although **2**-Cu(II) did not show fluorescence enhancement by addition of PPi, the electronic absorption was gradually changed with isosbestic points at 245 and 385 nm, indicating that the PPi successfully works as an ancillary ligand to the $Cu^{2+}$ (Figure S9). Because the maximum coordination number of $Cu^{2+}$ is six, additional ligands can be bound to the square planar **1**-Cu(II) complex to form the octahedral geometry. The square planar Cu(II) complexes can accommodate monodentate ligands without distortion of the square planar geometry by means of axial coordination. However, the square planar geometry should be distorted to form the octahedral geometry when bidentate ligand was coordinated to the Cu(II) complex (Figure 12). Unlike other anionic species, PPi can coordinate to metal ions as bidentate ligand. Therefore, the square planar geometry of Cu(II)-coordinated **BB** should be distorted by the coordination of PPi, which eventually reduces the aromaticity of Cu(II)-coordinated **BB**. In fact, the electronic absorption of **2**-Cu(II) in long wavelength region ($\lambda$ > 400 nm) was gradually reduced by the successive addition of PPi, indicating the increase of HOMO−LUMO band gap (Figure S9). Such changes may influence the energy transfer process from $\mathbf{P}_{Zn}$'s to the Cu(II)-coordinated **BB**. Because the excitation energy of


dx.doi.org/10.1021/ja4124048 | J. Am. Chem. Soc. 2014, 136, 1672−1679

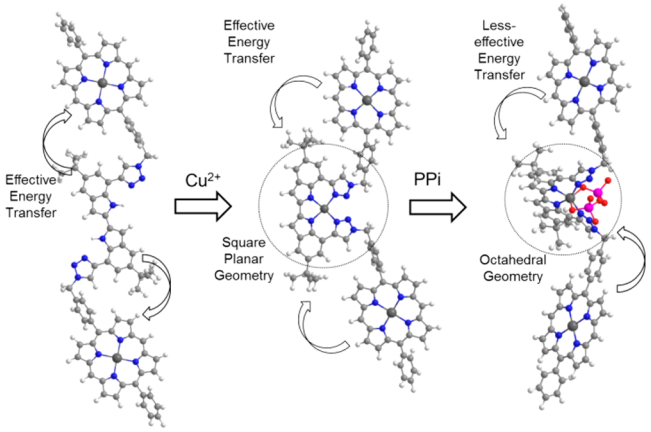


**Figure 12.** Proposed mechanism of fluorescence changes in **1** with energy minimized model calculated by MM2 force field.

Cu(II)-coordinated **BB** becomes higher by the PPi coordination, the energy transfer efficiency would eventually be decreased. To confirm this hypothesis, 2,2-bipyridine, and 1,3-bis(diphenylphosphino)propane, as other potential bidentate ligands, have been added to **1**-Cu(II) and **2**-Cu(II) complexes (Figure S10). Although the degree of fluorescence enhancement showed a large deviation, those molecules also exhibited similar fluorescence enhancement and decrease of absorption in long wavelength region, indicating the distortion of square planar geometry is caused by coordination of bidentate ligands. Therefore, we can conclude here that the energy transfer process from $\mathbf{P_{Zn}}$'s to **BB** can be further controlled by the coordination of bidentate ligands into the $Cu^{2+}$-coordinated **BB**.

## CONCLUSIONS

A bisindole-bridged-porphyrin tweezer exhibited a unique switching behavior in forward and backward photoinduced energy transfer by specific guest bindings. Because the fluorescence emission of **BB** well overlaps with the B band absorption of $\mathbf{P_{Zn}}$, effective Förster type energy transfer takes place from **BB** to $\mathbf{P_{Zn}}$'s. However, the direction of energy flow is completely reversed by the coordination of $Cu^{2+}$ into **BB**. The square planar Cu(II) complex of **BB** becomes a new energy acceptor, and $\mathbf{P_{Zn}}$'s become energy donors. Moreover, the binding of bidentate ligands to Cu(II)-coordinated **BB** decreases the energy flow from $\mathbf{P_{Zn}}$'s to **BB**. Therefore, we can demonstrate that the energy flow of the bisindole-bridged-porphyrin tweezer was successfully controlled by a guest specific manner. This active control of energy flow would be the best biomimetic model as well as a strong motif for the design of photofunctional nanodevices.

## ASSOCIATED CONTENT

### Supporting Information

Additional spectral data (Figures S1−10). This material is available free of charge via the Internet at http://pubs.acs.org.

## AUTHOR INFORMATION

### Corresponding Authors

wdjang@yonsei.ac.kr
dongho@yonsei.ac.kr

### Notes

The authors declare no competing financial interest.

## ACKNOWLEDGMENTS

This work was supported by the Midcareer Researcher programs (No. 2012005565 and 2010-0029668) and the Global Frontier R&D Program on Center for Multiscale Energy System (2012-8-2081) funded by the National Research Foundation under the Ministry of Science, ICT & Future, Korea. The quantum calculations were performed by using the supercomputing resources of the Supercomputing Center/Korea Institute of Science and Technology Information (KISTI).

## REFERENCES

(1) Liu, Z.; Yan, H.; Wang, K.; Kuang, T.; Zhang, J.; Gui, L.; An, X.; Chang, W. *Nature* **2004**, *428*, 287.
(2) McDermott, G.; Prince, S.; Freer, A.; Hawthornthwaite-Lawless, A.; Papiz, M.; Cogdell, R.; Isaacs, N. *Nature* **1995**, *374*, 517.
(3) Standfuss, J.; van Scheltinga, A. C. T.; Lamborghini, M.; Kühlbrandt, W. *EMBO J.* **2005**, *24*, 919.
(4) Hu, X.; Damjanović, A.; Ritz, T.; Schulten, K. *Proc. Natl. Acad. Sci. U.S.A.* **1998**, *95*, 5935.
(5) Choi, M. S.; Yamazaki, T.; Yamazaki, I.; Aida, T. *Angew. Chem., Int. Ed.* **2004**, *43*, 150.
(6) Van Patten, P. G.; Shreve, A. P.; Lindsey, J. S.; Donohoe, R. J. *J. Phys. Chem. B* **1998**, *102*, 4209.
(7) Aratani, N.; Kim, D.; Osuka, A. *Acc. Chem. Res.* **2009**, *42*, 1922.
(8) Jang, W.-D.; Lee, C.-H.; Choi, M.-S.; Osada, M. *J. Porphyrins Phthalocyanines* **2009**, *13*, 787.
(9) Kim, D.; Heo, J.; Ham, S.; Yoo, H.; Lee, C.-H.; Yoon, H.; Ryu, D.; Kim, D.; Jang, W.-D. *Chem. Commun.* **2011**, *47*, 2405.
(10) Son, K. J.; Yoon, H. J.; Kim, J. H.; Jang, W. D.; Lee, Y.; Koh, W. G. *Angew. Chem., Int. Ed.* **2011**, *50*, 11968.
(11) Hasobe, T.; Imahori, H.; Kamat, P. V.; Ahn, T. K.; Kim, S. K.; Kim, D.; Fujimoto, A.; Hirakawa, T.; Fukuzumi, S. *J. Am. Chem. Soc.* **2005**, *127*, 1216.
(12) Hasobe, T.; Kashiwagi, Y.; Absalom, M. A.; Sly, J.; Hosomizu, K.; Crossley, M. J.; Imahori, H.; Kamat, P. V.; Fukuzumi, S. *Adv. Mater.* **2004**, *16*, 975.
(13) Bessho, T.; Zakeeruddin, S. M.; Yeh, C. Y.; Diau, E. W. G.; Grätzel, M. *Angew. Chem., Int. Ed.* **2010**, *49*, 6646.
(14) Haider, J. M.; Williams, R. M.; De Cola, L.; Pikramenou, Z. *Angew. Chem., Int. Ed.* **2003**, *42*, 1830.
(15) Lammi, R. K.; Ambroise, A.; Balasubramanian, T.; Wagner, R. W.; Bocian, D. F.; Holten, D.; Lindsey, J. S. *J. Am. Chem. Soc.* **2000**, *122*, 7579.
(16) Niyogi, K. K.; Björkman, O.; Grossman, A. R. *Proc. Natl. Acad. Sci. U.S.A.* **1997**, *94*, 14162.
(17) Pascal, A. A.; Liu, Z.; Broess, K.; van Oort, B.; van Amerongen, H.; Wang, C.; Horton, P.; Robert, B.; Chang, W.; Ruban, A. *Nature* **2005**, *436*, 134.
(18) Anderson, J. M.; Park, Y. I.; Chow, W. *Physiol. Plant.* **1997**, *100*, 214.
(19) McConnell, I.; Li, G.; Brudvig, G. W. *Chem. Biol.* **2010**, *17*, 434.
(20) Kim, J. H.; Lee, M.; Lee, J. S.; Park, C. B. *Angew. Chem., Int. Ed.* **2012**, *51*, 517.
(21) Peng, H. Q.; Chen, Y. Z.; Zhao, Y.; Yang, Q. Z.; Wu, L. Z.; Tung, C. H.; Zhang, L. P.; Tong, Q. X. *Angew. Chem.* **2012**, *124*, 2130.
(22) Green, R. R.; Pichersky, E. *Photosynth. Res.* **1994**, *39*, 149.
(23) Joo, T.; Jia, Y.; Yu, J.-Y.; Jonas, D. M.; Fleming, G. R. *J. Phys. Chem.* **1996**, *100*, 2399.
(24) Ghanotakis, D. F.; Topper, J. N.; Babcock, G. T.; Yocum, C. F. *FEBS Lett.* **1984**, *170*, 169.
(25) Kruse, O.; Zheleva, D.; Barber, J. *FEBS Lett.* **1997**, *408*, 276.
(26) Vassiliev, I. R.; Kolber, Z.; Wyman, K. D.; Mauzerall, D.; Shukla, V. K.; Falkowski, P. G. *Plant Physiol.* **1995**, *109*, 963.
(27) Kimura, Y.; Hirano, Y.; Yu, L.-J.; Suzuki, H.; Kobayashi, M.; Wang, Z.-Y. *J. Biol. Chem.* **2008**, *283*, 13867.

(28) Helms, A.; Heiler, D.; McLendon, G. *J. Am. Chem. Soc.* **1992**, *114*, 6227.
(29) Priyadarshy, S.; Therien, M. J.; Beratan, D. N. *J. Am. Chem. Soc.* **1996**, *118*, 1504.
(30) Gust, D.; Moore, T. A.; Moore, A. L. *Acc. Chem. Res.* **1993**, *26*, 198.
(31) Kurreck, H.; Huber, M. *Angew. Chem., Int. Ed. Engl.* **1995**, *34*, 849.
(32) Ward, M. D. *Chem. Soc. Rev.* **1997**, *26*, 365.
(33) Marchi, E.; Baroncini, M.; Bergamini, G.; Van Heyst, J.; Vögtle, F.; Ceroni, P. *J. Am. Chem. Soc.* **2012**, *134*, 15277.
(34) Kim, P.; Sung, J.; Uoyama, H.; Okujima, T.; Uno, H.; Kim, D. *J. Phys. Chem. B* **2011**, *115*, 3784.
(35) Lim, J. M.; Inoue, M.; Sung, Y. M.; Suzuki, M.; Higashino, T.; Osuka, A.; Kim, D. *Chem. Commun.* **2011**, *47*, 3960.
(36) Fery-Forgues, S.; Lavabre, D. *J. Chem. Educ.* **1999**, *76*, 1260.
(37) Chang, K. J.; Moon, D.; Lah, M. S.; Jeong, K. S. *Angew. Chem.* **2005**, *117*, 8140.
(38) Connors, K. A. *Binding Constants: The Measurement of Molecular Complex Stability*; Wiley: New York, 1987.
(39) Peng, Y.; Li, Z.; Niu, Z.; Liu, Y.; Zeng, X.; Luo, Q.; Hughes, D. L.; Liu, X. *Inorg. Chim. Acta* **2009**, *362*, 3975.
(40) Karabıyık, H.; Erdem, Ö.; Aygün, M.; Güzel, B.; García-Granda, S. *J. Inorg. Organomet. Polym. Mater.* **2010**, *20*, 142.
(41) Harriman, A. *J. Chem. Soc., Faraday Trans. 2* **1981**, *77*, 1281.